RSC Advances

PAPER

View Article Online
View Journal | View Issue

Cite this: *RSC Adv.*, 2026, **16**, 11391

The onset of collective diffusion in hcp-iron: a combined theory of soft-matter and solid-state physics

Tran Dinh Cuong *[a] and Anh D. Phan [abc]

Received 10th January 2026
Accepted 18th February 2026

DOI: 10.1039/d6ra00258g

rsc.li/rsc-advances

Lately, scientists have discovered the existence of collective diffusion in hcp-iron *via* machine-learning algorithms. This result has opened a promising avenue for geophysical studies on planetary cores. However, the crossover between collective and non-collective regimes remains very ambiguous. Based on the solid–liquid similarity, we develop a simple differential equation to infer the crossover temperature from the density scaling exponent, the isothermal bulk modulus, and the volumetric thermal expansivity. All necessary thermodynamic inputs are provided by the statistical moment method for nonlinear atomic vibrations. Our theoretical results are supported by the latest computational data on warm-dense iron crystals. From there, we find a possible explanation for prolonged controversies about melting relations in diamond-anvil-cell experiments. The potential impacts of collective diffusion on the core properties of icy, rocky, and gaseous planets are also considered by combining our mineral-physics calculations with modern geodynamic models.

1 Introduction

Recently, collective dynamics has emerged as an attractive hotspot in planetary science.[1–3] It refers to the appearance of liquid-like mobile ions in crystalline solids under severe pressure–temperature (*P*–*T*) conditions. In the collective regime, crystals possess higher self-diffusivity, better ionic conductivity, and easier shear deformability. These interesting properties have significantly improved our understanding of chemical distribution, dynamo generation, and mechanical deformation inside icy, rocky, and gaseous worlds.[4–6]

Notably, the signature aspects of collective diffusion have been found in iron, the most bountiful metallic element in planetary cores. Using both *ab initio* and quasi-*ab initio* molecular dynamics, Belonoshko *et al.*[7] observed the shuffle of crystallographic planes in the bcc structure. This collective effect gave bcc-iron numerous unique properties, such as ultra-low viscosity and ultra-high Poisson ratio.[8,9] Inspired by the impressive results of Belonoshko's group, Cuong and Phan[10] developed the elastically collective nonlinear Langevin equation (ECNLE) to speed up computational processes and highlight the liquid-like behaviors of bcc-iron. They demonstrated that the inclusion of bcc fillers could satisfactorily explain the shear attenuation of Earth's inner core. Before long, Smirnov *et al.*[11] introduced a machine-learning force field for iron. Their computational model provided a deeper insight into solid–solid and solid–liquid transitions under super-Earth conditions, thereby facilitating research projects on extrasolar life.

However, the intrinsic stability of the pure bcc phase remains questionable. To date, only two experimental studies have supported the existence of bcc-iron.[12,13] The rest have claimed no observation of the bcc structure at elevated pressures and temperatures, regardless of using shock-wave, ramp-wave, or diamond-anvil-cell techniques.[14–18] This instability has also been recorded in various *ab initio*, quasi-*ab initio*, and machine-learning computations.[19–23] Although the kinetics of structural transformations, the uncertainty of interatomic potentials, and the oversymmetrization of simulated boxes have possibly clouded the bcc domain,[24] the above controversies have motivated the search for collective dynamics in other iron polymorphs.

In that context, Zhang *et al.*[25] discovered the formation of open-loop and closed-loop atomic clusters near the hcp-liquid boundary of iron *via* machine-learning molecular dynamics (MLMD). It had been thought for a long time that hcp atoms diffuse very weakly in the high-energy-density regime.[8] Nevertheless, according to Zhang *et al.*,[25] this physical picture would be broken down by the influence of point defects. Vacancies were able to form under the extreme heat of planetary cores and promote collective motion in the warm-dense hcp lattice. Instead of vibrating around fixed nodes, hcp atoms rapidly migrated along [100] or [010] directions to generate string-like structures. This phenomenon made hcp-iron become

[a]*Phenikaa Institute for Advanced Study, Phenikaa University, Yen Nghia, Ha Dong, Hanoi 12116, Vietnam. E-mail: cuong.trandinh@phenikaa-uni.edu.vn*
[b]*Faculty of Materials Science and Engineering, Phenikaa School of Engineering, Phenikaa University, Yen Nghia, Ha Dong, Hanoi 12116, Vietnam*
[c]*Center for Materials Innovation and Technology, VinUniversity, Hanoi 100000, Vietnam*

surprisingly soft, consistent with shock-wave measurements. Based on the diffusion-induced shear softening, Zhang *et al.*[25] offered a plausible explanation for abnormal seismic signals from Earth's center. Note that most experimental and computational evidence available today supports the stability of hcp-iron in planetary interiors.[14–23] Therefore, details about its collectivity are essential to elucidate geodynamic processes inside icy, rocky, and gaseous worlds.

The first step in exploring the collective regime is to find the crossover temperature T_c, at which iron atoms start to leave their equilibrium positions. Since the analytical expression of T_c remains unformulated, one can only estimate its value by tracking the time evolution of mean-square displacements (MSDs) at different P–T points.[25] If MSDs remain unchanged, collective diffusion will not take place in the studied supercell. If MSDs increase linearly during the simulated period, the crystal can gain liquid-like mobility at the atomistic level. Despite sounding simple, this dynamical method requires extensive and prolonged simulations to ensure the convergence of MSDs.[7–9] Thousands or even millions of metallic particles need to be scrutinized from femtoseconds to nanoseconds to avoid finite-size and finite-time effects. Due to prohibitive computational costs, all existing data for collective dynamics in hcp-iron are limited to 330 GPa.[25] This limit is insufficient to cover the physics of super-Earths and giant planets, whose internal pressures can exceed 1000 GPa.[26,27] Hence, an alternative approach is necessary to evaluate the impacts of collective diffusion on the past, present, and future of celestial bodies.

To meet the need, we combine the density scaling law (DSL) and the statistical moment method (SMM) to predict the onset of collective motion in hcp-iron without strenuous computational efforts. Our combination relies on the close similarity between pre-melting solids and glass-forming liquids.[28–31] While the DSL allows us to connect the crossover temperature T_c with the bulk modulus B_T and the thermal expansivity β_P *via* simple analytical formulas in soft-matter physics,[32] the SMM enables us to determine the P–T dependence of thermodynamic quantities *via* basic statistical tools in solid-state physics.[33] Our DSL-SMM calculations are applied to revisit heated debates about the melting process of iron in practical experiments.[34–36] Additionally, the ECNLE theory is used to decipher the unusual shear deformation of Earth's inner core.[10] To demonstrate the broad applicability of collective dynamics, we also make open predictions of the core state of super-Earths and solar giants by comparing the DSL-SMM phase boundary with planetary thermal profiles.[26,27] We hope our article can give the readers a compelling picture of hcp-iron and its geophysical applications in the collective regime.

2 Calculation

2.1. Formulation of crossover temperature

Let us express our physical ideas in more detail. Overall, crystalline materials exhibit both solid- and liquid-like behaviors when the collective diffusion of ions is triggered at elevated temperatures.[28,29] This characteristic vividly reminds us of glass formers in the field of soft matter. Modern atomistic simulations have recorded numerous hallmarks of glass-forming liquids in pre-melting crystals at the microscopic level, such as intrinsic heterogeneity, dynamic facilitation, and string formation.[30,31,37–40] The above studies have also revealed the applicability of simple glass models (*e.g.*, the localization equation[41] and the Adam–Gibbs theory[42]) to describe collective effects during heating. In particular, ECNLE researchers have successfully modeled the structural relaxation, ionic transportation, and mechanical deformation of fast-ion solids inside planetary cores and nuclear reactors, including bcc-iron, uranium oxide, and mixed oxide fuel.[10,43] Thus, it is viable to leverage the reservoir of knowledge about vitrification to shed light on the transition between collective and non-collective states.

In many cases, vitrification and collectivization are quite similar to second-order phase transitions in equilibrium thermodynamics. Although the volume V grows continuously with increasing temperature, its first derivative shows a discontinuity near the crossover point.[1,6,44] This event suggests that the T_c–P relation may obey the Ehrenfest equation,[45]

$$\frac{\mathrm{d}T_c}{\mathrm{d}P} = VT_c\frac{\Delta\beta_P}{\Delta C_P}, \tag{1}$$

where Δ denotes abrupt changes in the heat capacity C_P and the thermal expansivity β_P. The entropy approach of Ehrenfest has been widely applied to polymer melts, amorphous drugs, and superionic crystals.[46,47] However, this is not an ideal choice for the present situation. The principal reason is that eqn (1) incorporates physical quantities before and after collectivization. As introduced in Section 1, thermodynamic calculations become highly demanding when mobile atoms leave lattice nodes to engage in collective loops. To optimize computational time and cost, we need to devise another strategy for accessing the phase boundary of hcp-iron at extreme pressures and temperatures.

Remarkably, according to recent ECNLE analyses,[10,43] vitrification and collectivization can be viewed as isochronal processes. In other words, the object of study will begin to kinetically vitrify or collectively diffuse if its structural relaxation time reaches a critical value. This isochronal criterion is equivalent to the DSL picture of molecular dynamics[48–50]

$$TV^{\gamma} = \text{const}, \tag{2}$$

where γ is a microscopic parameter originating from the pressure–energy correlation of material. Specifically, γ characterizes the steepness of the short-range repulsive interaction between atoms.[51–53] It can be determined by fitting numerical results for the interatomic potential φ with the inverse-power-law function φ_{IPL},[54]

$$\varphi_{\mathrm{IPL}} = \frac{C}{r^{3\gamma}} + A, \tag{3}$$

where r is the nearest neighbor distance, C is the repulsive constant, and A is the attractive background. Since γ is frequently supposed to be independent of P and T,[32,46,55,56] we can rewrite eqn (2) in the differential form as

$$V^{\gamma} + \gamma TV^{\gamma-1}\left[\left(\frac{\partial V}{\partial T}\right)_P + \left(\frac{\partial V}{\partial P}\right)_T\frac{\mathrm{d}P}{\mathrm{d}T}\right] = 0. \tag{4}$$

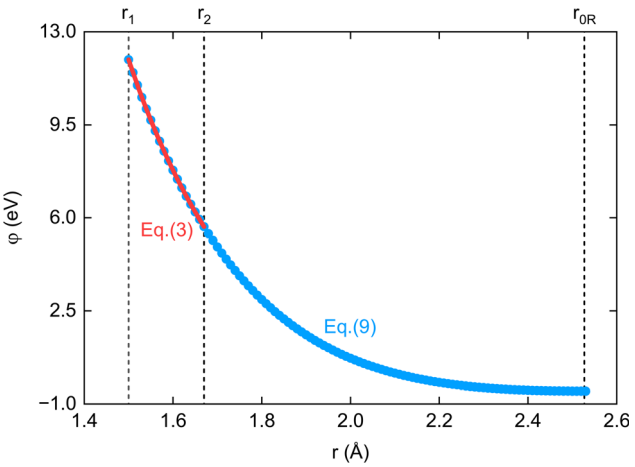

Fig. 1 The interatomic interaction in hcp-iron provided by the first-principle-based Rydberg model [eqn (9)] and the inverse-power-law potential [eqn (3)].

Note that the bulk modulus B_T and the thermal expansivity β_P are defined by

$$B_T = -V\left(\frac{\partial P}{\partial V}\right)_T, \tag{5}$$

$$\beta_P = \frac{1}{V}\left(\frac{\partial V}{\partial T}\right)_P. \tag{6}$$

Eqn (5) and (6) help us simplify eqn (4) to

$$\frac{\mathrm{d}T_c}{\mathrm{d}P} = \frac{\gamma T_c}{B_T(1+\gamma T_c \beta_P)}. \tag{7}$$

Unlike eqn (1) and (7) only uses thermodynamic data in the normal crystalline state, which is readily accessible by available experimental, computational, and theoretical techniques. Hence, we consider eqn (7) a key to illuminating the collective motion of hcp-iron in planetary interiors. The starting point is selected at 5000 K and 220 GPa, corresponding to the lower limit of prior MLMD simulations.[25]

2.2. Determination of thermodynamic inputs

To calculate the right-hand side of eqn (7), we employ the SMM model in quantum statistical mechanics. This analytical model has been demonstrated to be advantageous for capturing high-energy-density physics in different structures.[57–59] The SMM divides the total vibrational free energy F_{vib} into three principal parts: (i) static (F_0), (ii) quasi-harmonic (F_{qh}), and (iii) anharmonic (F_{ah}). Interestingly, if we know F_0 from experiments or simulations, we can readily infer F_{qh} and F_{ah} from the SMM recurrence formula for displacement moments.[60–62] This self-consistent approach allows us to speed up computational processes without sacrificing accuracy. Details about SMM free-energy calculations for hcp-iron were carefully reported by Cuong and Phan.[33] Here, we only present fundamental steps to obtain γ, B_T, and β_P.

First, we use four coordination shells in the hcp lattice to express F_0 as

$$F_0 = 6\varphi(r) + 3\varphi\left(r\sqrt{2}\right) + \varphi\left(r\sqrt{8/3}\right) + 9\varphi\left(r\sqrt{3}\right). \tag{8}$$

The roaring success of the Vinet equation of state in describing the isotherms and isentropes of transition metals motivates us to parametrize $\varphi(r)$ by[63–65]

$$\varphi(r) = -D_R[1 + b_R(r - r_{0R})]\exp[-b_R(r - r_{0R})], \tag{9}$$

where $D_R = 0.524851$ eV, $b_R = 2.56479$ Å^{-1}, and $r_{0R} = 2.52699$ Å are the Rydberg parameters derived from the linearized-augmented plane-wave method.[66] Eqn (9) enables us to satisfactorily explain low-temperature physical processes in hcp-iron, such as hydrostatic densification, sound-wave propagation, and structural transformation.[33] Moreover, we can quantify the scaling exponent γ of hcp-iron by combining eqn (9) with eqn (3). Fig. 1 shows that the interaction between iron atoms in the hcp phase is perfectly modeled by the inverse power law from $r_1 = 1.50$ Å to $r_2 = 1.67$ Å. Our fitting range is selected based on the recommendation of Koperwas *et al.*[54] to avoid the overestimation of γ. While r_1 is the shortest distance our potential can approach, r_2 satisfies

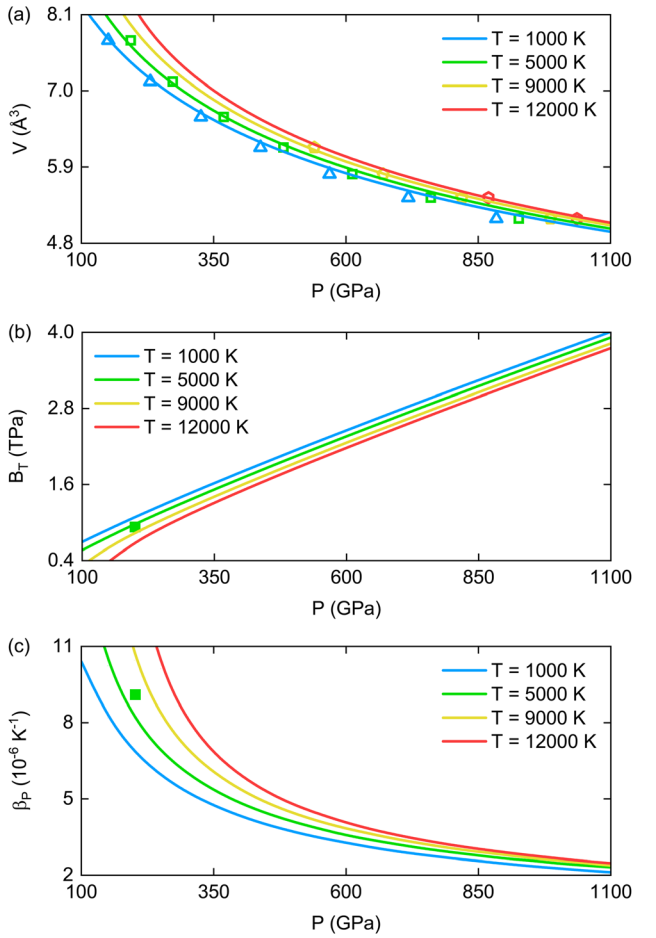

Fig. 2 The atomic volume (a), the bulk modulus (b), and the thermal expansivity (c) of hcp-iron. Solid lines: SMM calculations, empty symbols: *ab initio* molecular dynamics simulations,[17] filled symbols: single-shock experiments.[70,71]

$$\varphi(r_2) = \varphi(r_1) - \frac{1}{2}[\varphi(r_1) - \varphi(r_{0R})]. \quad (10)$$

Because the upper limit of the cold isotherm in the Rydberg model is $P_1 = 10.2$ TPa,[67] r_1 is estimated by

$$P_1 = -\frac{\sqrt{2}}{3{r_1}^2}\left(\frac{dF_0}{dr}\right)_{r=r_1}. \quad (11)$$

The above procedure gives us $\gamma = 1.57$.

Next, we utilize F_0 to handle F_{qh} and F_{ah}. According to the vibrational theory of Leibfried and Ludwig,[68] it is feasible to calculate the quasi-harmonic coupling parameter (k) and its anharmonic counterparts (β, γ_1, γ_2) by

$$k = \left(\frac{\partial^2 F_0}{\partial {u_\xi}^2}\right)_{eq}, \quad \beta = \left(\frac{\partial^3 F_0}{\partial u_\xi \partial {u_\eta}^2}\right)_{eq},$$

$$\gamma_1 = \frac{1}{24}\left(\frac{\partial^4 F_0}{\partial {u_\xi}^4}\right)_{eq}, \quad \gamma_2 = \frac{1}{4}\left(\frac{\partial^4 F_0}{\partial {u_\xi}^2 \partial {u_\eta}^2}\right)_{eq}, \quad (12)$$

where u_ξ and u_η describe atomic displacements in the Cartesian coordinate system ($\xi \neq \eta = x, y, z$). Analytical results for k, β, γ_1, and γ_2 are detailed in Appendix A. Since k is the product of the atomic mass m and the squared Einstein frequency ${\omega_E}^2$, we can approximate the quasi-harmonic free energy of hcp-iron by

$$F_{qh} = \frac{3}{2}\hbar\omega_E + 3\theta \ln\left[1 - \exp\left(-\frac{\hbar\omega_E}{\theta}\right)\right], \quad (13)$$

where θ is the Boltzmann thermal energy, and $\hbar$ is the reduced Planck constant.[69] Besides, the contribution of nonlinear atomic fluctuations is quantified by the following thermodynamic integral[33]

$$F_{ah} = 3\int_0^{\beta} \langle u_\xi \rangle \langle {u_\eta}^2 \rangle d\beta + 3\int_0^{\gamma_1} \langle {u_\xi}^4 \rangle d\gamma_1 + 3\int_0^{\gamma_2} \langle {u_\xi}^2 \rangle \langle {u_\eta}^2 \rangle d\gamma_2, \quad (14)$$

where angle brackets denote average values in the equilibrium state. It should be noted that all displacement moments in the SMM model are tightly connected *via* the quantum density matrix.[60–62] Thus, we can rapidly compute $\langle {u_\xi}^2 \rangle$ and $\langle {u_\xi}^4 \rangle$ after gaining $\langle u_\xi \rangle$ from the force-balance condition. This connection results in the explicit form of eqn (14),

$$F_{ah} = \frac{\theta^2}{K^2}\left[3\gamma_2 X^2 - \gamma_1(X+2)\right] + \frac{2\theta^3}{K^4}(X+2)\left[2{\gamma_2}^2 X - 3\gamma_1(\gamma_1 + 2\gamma_2)(X+1)\right] + \frac{3\beta\theta^2}{K}\left[\frac{4(\gamma_1+\gamma_2)}{3K^3}(X+2)\right]^{\frac{1}{2}} + 3\beta\theta^3\left\{\left[\frac{4(\gamma_1+\gamma_2)}{3K^3}(X+2)\right]^{\frac{3}{2}} + \frac{8k(\gamma_1+\gamma_2)}{K^6}\beta\right\}, \quad (15)$$

where $K = k - \dfrac{\beta^2}{12(\gamma_1+\gamma_2)}$ and $X = \dfrac{\hbar\omega_E}{2\theta}\coth\dfrac{\hbar\omega_E}{2\theta}$.

Finally, the total vibrational free energy is given by

$$F_{vib} = F_0 + F_{qh} + F_{ah}. \quad (16)$$

Eqn (16) is beneficial for investigating the geophysical properties of warm-dense iron along melting lines, shock Hugoniots, ramp isentropes, and solid–solid boundaries.[33] It also helps us derive the equation of state from

$$P = -\left(\frac{\partial F_{vib}}{\partial V}\right)_T. \quad (17)$$

As illustrated in Fig. 2(a), our SMM analyses agree quantitatively well with previous *ab initio* molecular dynamics simulations.[17] No errors in the atomic volume V exceed 2.5% in the examined region ($1000 \leq T \leq 12\,000$ K and $100 \leq P \leq 1100$ GPa). Therefore, we can confidently calculate the bulk modulus B_T and the thermal expansivity β_P of hcp-iron in severe environments by combining eqn (17) with eqn (5) and (6). Our conclusion is strengthened by single-shock experiments in Fig. 2(b) and (c).[70,71]

2.3. Validation of theoretical model

Fig. 3 depicts how the crossover temperature of hcp-iron depends on pressure. It is conspicuous that T_c experiences a continuous increase during squeezing. Theoretically, when hcp-iron is compressed from 0 to 1000 GPa, T_c is expected to climb from 2669 to 8775 K. This growth is flawlessly consistent with the large-scale, long-time atomistic simulations of Zhang *et al.*[25] None of our outputs violates MLMD constraints in a pressure range between 230 and 330 GPa. We believe these computational constraints are relatively tight because Zhang *et al.*[25] carefully handled finite-size and finite-time problems in the MSDs method. More than 10 000 iron atoms were simulated from femtosecond to nanosecond timescales to ensure the convergence of the crossover temperature. The excellent agreement above confirms the efficiency and accuracy of our newly developed analytical approach. Its quality is further validated in the case of bcc-iron (see Appendix B). To facilitate the

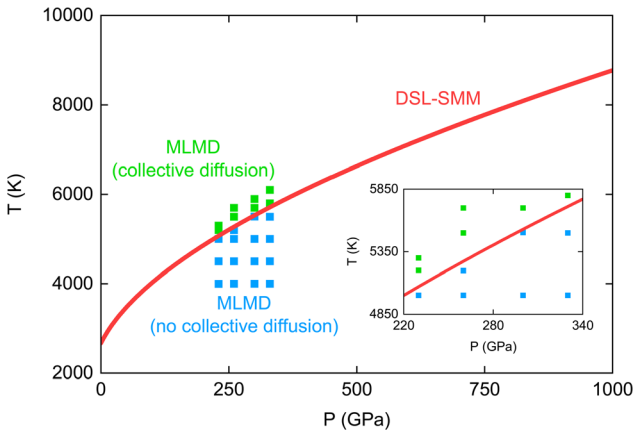

Fig. 3 The crossover temperature of hcp-iron as a function of pressure obtained from present DSL-SMM calculations and previous MLMD computations.[25] (Inset) Zooming in on the previously simulated region.

journey of Earth and space exploration, we parametrize our dynamic phase boundary by the empirical law of Simon and Glatzel,[72]

$$T_c = c_1\left(1+\frac{P}{c_2}\right)^{\frac{1}{c_3}}, \tag{18}$$

where $c_1 = 2669$ K, $c_2 = 65.04$ GPa, and $c_3 = 2.36$ are fitting parameters.

3 Implication

3.1. The never-ending story of iron melting curve

Eqn (18) allows us to compare the onsets of collective diffusion and melting transition in Fig. 4. After meticulously reviewing diamond-anvil-cell data between 1993 and 2018, Morard *et al.*[73] reported three different scenarios for the melting line of iron: (a) flat,[34,74] (b) neutral,[75,76] and (c) steep.[35] Whereas scenario (a) was ascribed to chemical contamination, scenario (b) was attributed to pressure overestimation. Morard *et al.*[73] highly recommended scenario (c), in which the melting temperature of iron would reach 6230 K at the Earth's inner core boundary. Nevertheless, in 2019, Sinmyo *et al.*[36] gathered a lot of supporting evidence for scenario (b) from resistance-heated diamond-anvil-cell experiments. Their experimental results suggested that iron would melt at 5500 K and 330 GPa. Although numerous attempts have been made, the geophysical community has not found an adequate explanation for what Sinmyo *et al.*[36] observed.

In such situations, the DSL-SMM method becomes particularly useful. Fig. 4 shows that our crossover curve sits quite close to the intermediate melting points reported by Sinmyo *et al.*[36] This closeness warns: there may be confusion between "melting transition" and "collective diffusion" in practical experiments. Sinmyo *et al.*[36] established their melting criterion based on the saturation of temperature during voltage rising. Since collective effects help hcp-iron evacuate heat by both conduction and convection mechanisms, melting-like plateaus can be formed on voltage–temperature diagrams.[8,77] This phenomenon riskily creates the illusion of melting under extreme conditions. Hence, we deem scenario (c) still the most viable. Our conclusion is strengthened by recent shock-wave measurements for the phase relations of iron along Hugoniot branches.[15,16,18] However, it should be noted that our interpretation is only suitable for $P > 200$ GPa. At $P < 200$ GPa, the sample temperature of Sinmyo *et al.*[36] is too low to take into account the influences of collective diffusion. More experimental, computational, and theoretical efforts are required to gain a unified picture from low to high pressures. Some factors to consider include resistance variation, chromatic aberration, and impurity incorporation.[78,79]

3.2. The shear deformation of Earth's inner core

Besides heated debates about diamond anvil cells, it is essential to assess the significance of collective motions to geodynamic understandings. Take the shear properties of Earth's inner core as an example. Seismic observations have revealed that Earth's inner core is very soft. Its shear modulus G is only about 167 to 176 GPa in the central region.[80–82] These counterintuitive results have challenged seismologists and mineralogists for decades because iron—the main component of Earth's inner core—has been thought to be highly resistant to shear deformation. At $P = 360$ GPa and $T = 6000$ K, empirical extrapolations yield $G = 335$ GPa for the hcp structure.[83] A plethora of solutions have been proposed to untie the knot with the aid of melt pockets,[84] superheating effects,[85] alloying elements,[86] grain boundaries,[87] and bcc fillers.[10] Unfortunately, a strong consensus has not been reached due to unsolved questions about defect formation and phase stabilization.

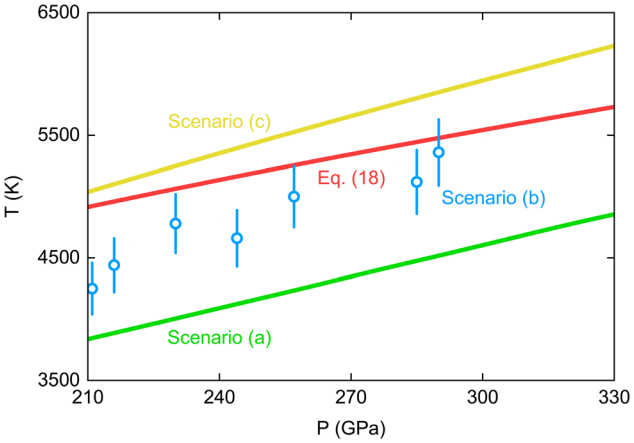

Fig. 4 Comparing the DSL-SMM transition curve of hcp-iron with its experimental solid–liquid boundaries. Scenario (a): flat melting,[34] scenario (b): neutral melting,[36] scenario (c): steep melting.[35]

Fortunately, the discovery of liquid-like mobile atoms in the hcp lattice can pave the way to escape this predicament. To reinforce our point of view, we estimate the shear modulus G of hcp-iron in the fast-ion state by the ECNLE theory.[10] This theory utilizes the hard-sphere fluid of Percus and Yevick[88] to rapidly determine the physical properties of soft materials at different packing fractions ϕ. By taking the sum of the Miller configurational rigidity[89] and the Khrapak kinetic rigidity,[90] we have

$$G = G_c\frac{\phi}{\phi_c}\frac{T}{T_c}\left[1+\frac{36}{5}\frac{\phi^2(1+\phi)}{(1-\phi)^3}\right]\left[1+\frac{36}{5}\frac{\phi_c{}^2(1+\phi_c)}{(1-\phi_c)^3}\right]^{-1}, \tag{19}$$

where the critical value $G_c = G(P, T_c)$ is inferred from the empirical model of Ikuta *et al.*[83] to ensure the continuity of G before and after collectivization.[25,91] It is practicable to convert ϕ into P and T *via* the following chemical mapping[92]

$$\phi = \frac{\phi_0\beta_0(T_c - T)}{1+\dfrac{6c_3+\sqrt{1+24c_3}-1}{c_2c_3\left(\sqrt{1+24c_3}+5\right)}P} + \phi_c, \tag{20}$$

where $\phi_0 = 0.5$, $\phi_c = 0.611$, and $\beta_0 = 12\times10^{-4}\ \mathrm{K}^{-1}$ are universal constants obtained by analyzing theoretical and experimental data for molecular, polymeric, and pharmaceutical systems. Eqn (20) is inspired by the reduction of particle density during heating and the similarity between melting, vitrification, and collectivization. Its effectiveness was carefully validated by *ab*

initio data for bcc-iron.[9,10] As illustrated in Fig. 5, collective effects strongly reduce the shear resistance of hcp-iron in the high-energy-density regime. Our ECNLE analyses indicate that G plunges nonlinearly to the seismic value at $T \approx 6400$ K and $P = 360$ GPa. This shear softening cannot be found in previous studies on ordinary hcp systems.[83,93,94] In particular, our investigated P–T conditions are highly relevant to Earth's inner core. We do not need unrealistic superheating degrees to match theoretical calculations with seismic observations.[80–82] Our physical picture is bolstered by recent shock-wave experiments in Appendix C. This encouraging result offers a bright prospect of unlocking long-standing enigmas in Earth science. It will be appealing if the influence of light elements (*e.g.*, H, C, O, Si, and S) on the collective diffusion of hcp-iron can be clarified in subsequent research projects to gain a more comprehensive description of inner-core structure, dynamics, and history.[95]

3.3. The core state of other planets

Notably, in recent years, the National Aeronautics and Space Administration has announced the existence of numerous super-Earths outside the Solar System.[96] These rocky exoplanets have attracted intense interest due to their potential habitability.[97] Modern experimental and computational works on planet-forming materials have suggested that the core crystallization of rocky worlds would happen from the bottom up.[58,98] Therefore, it is fascinating to consider whether super-Earth inner cores are in the fast-ion state. To answer this question, we add our dynamic boundary to the P–T phase diagram of iron constructed from cutting-edge diamond-anvil-cell and shock-wave data.[16,35] Besides, we estimate the inner-core temperature of super-Earths by the cryoscopic equation,

$$T_{\rm core} = \frac{T_{\rm m}}{1 - \ln(1 - x^*)}, \tag{21}$$

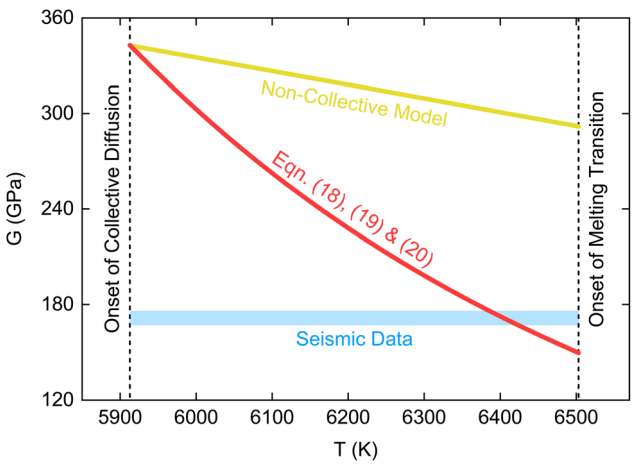

Fig. 5 Temperature effects on the shear modulus of hcp-iron given by our DSL-SMM-ECNLE approach and the non-collective extrapolation of Ikuta *et al.*[83] at 360 GPa. The melting point of hcp-iron is extracted from the dynamic measurements of Kraus *et al.*[16] to bound the stability field of fast-ion diffusion. Seismic data on Earth's solid inner core are also included to highlight the importance of collective dynamics.[80–82]

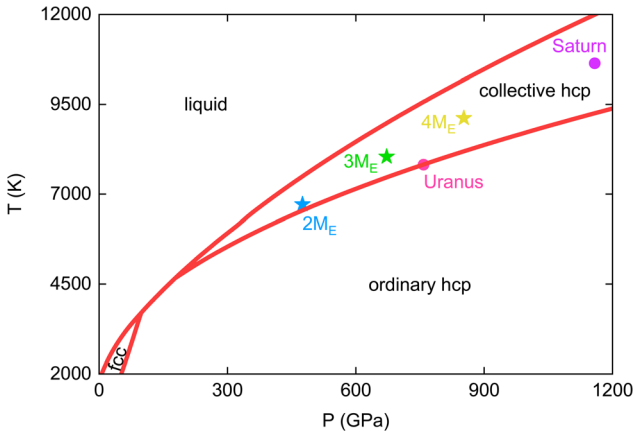

Fig. 6 Our proposed phase diagram for iron (solid lines). Also plotted are P–T points corresponding to the inner-core boundary of super-Earths (filled stars) and giant planets (filled circles).

where $T_{\rm m} = 5530\left[\frac{P-260}{293}+1\right]^{0.552}$ is the melting temperature of pure Fe,[16] and $x^* = 0.11$ is the mole fraction of other elements.[99] The inner-core pressure is directly taken from the compression profiles of Boujibar *et al.*[27] in a mass range from $2M_{\rm E}$ to $4M_{\rm E}$ ($M_{\rm E} = 5.9722 \times 10^{24}$ kg is Earth's mass). As presented in Fig. 6, we have $T_{\rm c} < T_{\rm core} < T_{\rm m}$. That is synonymous with the great possibility of finding hcp-iron with collective motion inside super-Earths. It has been demonstrated that the interaction between liquid-like mobile ions and electromagnetic fields can strongly affect the internal structure of planetary cores.[6] Accordingly, physicists should pay more attention to collective effects when developing geodynamic models for super-Earths. Our predicted diffusivity is reported in Appendix D.

Apart from rocky planets, the collective state also has a chance to exist inside ice and gas giants, whose temperature distributions were summarized by Mazevet *et al.*[26] For icy worlds (*e.g.*, Uranus and Neptune), the appearance of collective diffusion may generate dipolar dynamos by enhancing the electrical conductivity of solid inner cores.[100] In this situation, a stably stratified fluid layer is necessary to ensure the non-dipolar morphology of planetary magnetic fields.[101] For gaseous worlds (*e.g.*, Saturn and Jupiter), collectivization would significantly increase the solubility of hcp-iron in metallic hydrogen.[102] The consequence is that the core erosion may be much more severe than previously thought.[103] Hence, an accurate database of the geophysical properties of hcp-iron in the collective regime (*e.g.*, density, energy, diffusivity, and conductivity) is urgently needed to serve upcoming space missions related to giant planets.[104]

4 Conclusion

By coupling the density scaling law in soft-matter physics with the statistical moment method in solid-state physics, we have successfully developed a simple analytical approach to predict the onset of collective diffusion in hcp-iron from its

fundamental thermodynamic properties. An excellent concurrence between theory and simulation has been achieved in computationally accessible regions. From there, we have partially resolved long-standing controversies about the solid–liquid transition of iron and the shear deformation of Earth's inner core. Some open predictions of collective dynamics inside super-Earths and solar giants have also been provided to promote future works in planetary science. Our results have reaffirmed the close similarity between pre-melting solids and glass-forming liquids under various thermodynamic conditions. This similarity promises to bring innovative ways to optimize computational processes in the high-energy-density regime. Scientists can leverage well-known glass models, such as the elastically collective nonlinear Langevin equation, to rapidly compute the relaxation, transportation, and deformation quantities of fast-ion crystals within and beyond the Solar System.

5 Appendix A: vibrational coupling parameters

Employing the Leibfried–Ludwig expansion gives us

$$k = 2\frac{\mathrm{d}^2\varphi_1}{\mathrm{d}r^2} + \frac{4}{r}\frac{\mathrm{d}\varphi_1}{\mathrm{d}r} + \frac{1}{2}\frac{\mathrm{d}^2\varphi_2}{\mathrm{d}r^2} + \frac{1}{r}\frac{\mathrm{d}\varphi_2}{\mathrm{d}r} + \frac{3}{8r}\frac{\mathrm{d}\varphi_3}{\mathrm{d}r} + \frac{23}{18}\frac{\mathrm{d}^2\varphi_4}{\mathrm{d}r^2} + \frac{31}{18r}\frac{\mathrm{d}\varphi_4}{\mathrm{d}r},$$

$$\beta = \frac{\sqrt{3}}{12}\frac{\mathrm{d}^3\varphi_1}{\mathrm{d}r^3} - \frac{\sqrt{3}}{4r}\frac{\mathrm{d}^2\varphi_1}{\mathrm{d}r^2} + \frac{\sqrt{3}}{4r^2}\frac{\mathrm{d}\varphi_1}{\mathrm{d}r} - \frac{\sqrt{3}}{12}\frac{\mathrm{d}^3\varphi_2}{\mathrm{d}r^3} + \frac{\sqrt{3}}{4r}\frac{\mathrm{d}^2\varphi_2}{\mathrm{d}r^2} - \frac{\sqrt{3}}{4r^2}\frac{\mathrm{d}\varphi_2}{\mathrm{d}r} + \frac{5\sqrt{3}}{81}\frac{\mathrm{d}^3\varphi_4}{\mathrm{d}r^3} - \frac{5\sqrt{3}}{27r}\frac{\mathrm{d}^2\varphi_4}{\mathrm{d}r^2} + \frac{5\sqrt{3}}{27r^2}\frac{\mathrm{d}\varphi_4}{\mathrm{d}r},$$

$$\gamma_1 = \frac{5}{96}\frac{\mathrm{d}^4\varphi_1}{\mathrm{d}r^4} + \frac{3}{16r}\frac{\mathrm{d}^3\varphi_1}{\mathrm{d}r^3} + \frac{1}{32r^2}\frac{\mathrm{d}^2\varphi_1}{\mathrm{d}r^2} - \frac{1}{32r^3}\frac{\mathrm{d}\varphi_1}{\mathrm{d}r} + \frac{1}{192}\frac{\mathrm{d}^4\varphi_2}{\mathrm{d}r^4} + \frac{1}{32r}\frac{\mathrm{d}^3\varphi_2}{\mathrm{d}r^3} - \frac{1}{64r^2}\frac{\mathrm{d}^2\varphi_2}{\mathrm{d}r^2} + \frac{1}{64r^3}\frac{\mathrm{d}\varphi_2}{\mathrm{d}r} + \frac{9}{512r^2}\frac{\mathrm{d}^2\varphi_3}{\mathrm{d}r^2} - \frac{9}{512r^3}\frac{\mathrm{d}\varphi_3}{\mathrm{d}r} + \frac{179}{15\,552}\frac{\mathrm{d}^4\varphi_4}{\mathrm{d}r^4} + \frac{97}{2592r}\frac{\mathrm{d}^3\varphi_4}{\mathrm{d}r^3} - \frac{113}{5184r^2}\frac{\mathrm{d}^2\varphi_4}{\mathrm{d}r^2} + \frac{113}{5184r^3}\frac{\mathrm{d}\varphi_4}{\mathrm{d}r},$$

$$\gamma_2 = \frac{5}{48}\frac{\mathrm{d}^4\varphi_1}{\mathrm{d}r^4} + \frac{3}{8r}\frac{\mathrm{d}^3\varphi_1}{\mathrm{d}r^3} + \frac{1}{16r^2}\frac{\mathrm{d}^2\varphi_1}{\mathrm{d}r^2} - \frac{1}{16r^3}\frac{\mathrm{d}\varphi_1}{\mathrm{d}r} + \frac{1}{96}\frac{\mathrm{d}^4\varphi_2}{\mathrm{d}r^4} + \frac{1}{16r}\frac{\mathrm{d}^3\varphi_2}{\mathrm{d}r^3} - \frac{1}{32r^2}\frac{\mathrm{d}^2\varphi_2}{\mathrm{d}r^2} + \frac{1}{32r^3}\frac{\mathrm{d}\varphi_2}{\mathrm{d}r} + \frac{9}{256r^2}\frac{\mathrm{d}^2\varphi_3}{\mathrm{d}r^2} - \frac{9}{256r^3}\frac{\mathrm{d}\varphi_3}{\mathrm{d}r} + \frac{179}{7776}\frac{\mathrm{d}^4\varphi_4}{\mathrm{d}r^4} + \frac{97}{1296r}\frac{\mathrm{d}^3\varphi_4}{\mathrm{d}r^3} - \frac{113}{2592r^2}\frac{\mathrm{d}^2\varphi_4}{\mathrm{d}r^2} + \frac{113}{2592r^3}\frac{\mathrm{d}\varphi_4}{\mathrm{d}r}. \quad (22)$$

Here, φ_1, φ_2, φ_3, and φ_4 are expressed by

$$\varphi_1 = -D_\mathrm{R}[1 + b_\mathrm{R}(r - r_{0\mathrm{R}})]\exp[-b_\mathrm{R}(r - r_{0\mathrm{R}})],$$

$$\varphi_2 = -D_\mathrm{R}\left[1 + b_\mathrm{R}\left(r\sqrt{2} - r_{0\mathrm{R}}\right)\right]\exp\left[-b_\mathrm{R}\left(r\sqrt{2} - r_{0\mathrm{R}}\right)\right],$$

$$\varphi_3 = -D_\mathrm{R}\left[1 + b_\mathrm{R}\left(r\sqrt{8/3} - r_{0\mathrm{R}}\right)\right]\exp\left[-b_\mathrm{R}\left(r\sqrt{8/3} - r_{0\mathrm{R}}\right)\right],$$

$$\varphi_4 = -D_\mathrm{R}\left[1 + b_\mathrm{R}\left(r\sqrt{3} - r_{0\mathrm{R}}\right)\right]\exp\left[-b_\mathrm{R}\left(r\sqrt{3} - r_{0\mathrm{R}}\right)\right]. \quad (23)$$

6 Appendix B: the crossover temperature of bcc-iron

To strengthen our theoretical model, we conduct an additional investigation into bcc-iron, whose collective motions have been recorded by classical, quantum, and machine-learning computations.[7,105,106] Detailed information about our SMM calculations for the bcc structure can be found in ref. 107. Applying the fitting procedure of Koperwas *et al.*[54] to the extended Rydberg potential yields $\gamma = 2.20$. Entering this scaling exponent into eqn (2) with initial conditions of $P = 79$ GPa and $T_\mathrm{c} = 2833$ K (ref. 12) leads to Fig. 7. It is easy to see that our combined theory works very well in deep-planetary environments. At $P = 3300$ GPa, we obtain $T_\mathrm{c} = 18\,993$ K, consistent with $T_\mathrm{c} = 18\,500$ K gained from *ab initio* molecular dynamics simulations.[105] This quantitative consistency implies that the inverse-power-law approximation ($\gamma = \mathrm{const}$ (ref. 108)) is sufficiently accurate to model collective effects, at least in Earth and super-Earth ranges. Thus, we can be confident in the theoretical predictions presented in the main text.

7 Appendix C: theoretical *versus* experimental shear properties

Fig. 8 compares the DSL-SMM-ECNLE and shock-wave shear moduli of hcp-iron at 230 GPa. Overall, there is a good agreement between theory and experiment. Our analyses show that the appearance of collective motions reduces G from 170 to 142 GPa at 5180 K, similar to what Zhang *et al.*[25] reported ($G = 136$ GPa). This concurrence confirms that eqn (18)–(20) are appropriate for describing mechanical properties in the fast-ion state. Therefore, we can utilize them to explore the promising geophysical applications of hcp-iron above the crossover temperature.

8 Appendix D: the diffusion coefficient of hcp-iron

To promote the development of planetary models, we investigate the collective diffusion of hcp-iron at the microscopic level

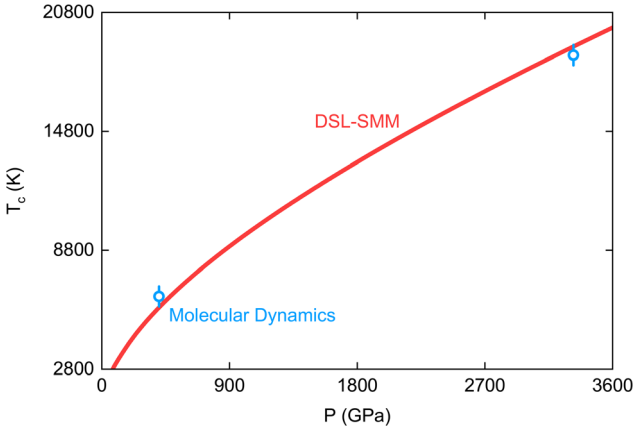

Fig. 7 The pressure dependence of the crossover temperature of bcc-iron given by our theoretical calculations and quantum simulations.[105]

by combining the ECNLE theory with the DSL-SMM method. Specifically, each iron atom in the fast-ion state is modeled by an impenetrable sphere with an effective diameter σ. Its free energy $F_{\rm dyn}$ is inferred from the nonensemble-averaged dynamic density functional theory,[109]

$$F_{\rm dyn} = -3\theta \ln\frac{r}{\sigma} - \theta\int\frac{{\rm d}\vec{q}}{(2\pi)^3}\frac{S}{\rho}\frac{\left(1-S^{-1}\right)^2}{1+S^{-1}}\exp\left[-\frac{q^2r^2}{6}\left(1+S^{-1}\right)\right], \quad (24)$$

where r is the spatial distance, q is the wave vector, ρ is the particle density, and S is the Percus–Yevick static structure factor. Note that $F_{\rm dyn}$ does not have an equilibrium thermodynamic meaning. This quantity is directly linked with the effective force acting on the studied sphere in the Langevin equation of motion. It captures not only Fickian dynamics (the first term) but also many-body caging effects (the second term). To break free from the neighboring cage and engage in the concerted migration, the sphere needs to transcend the entropic barrier $F_{\rm B}$,

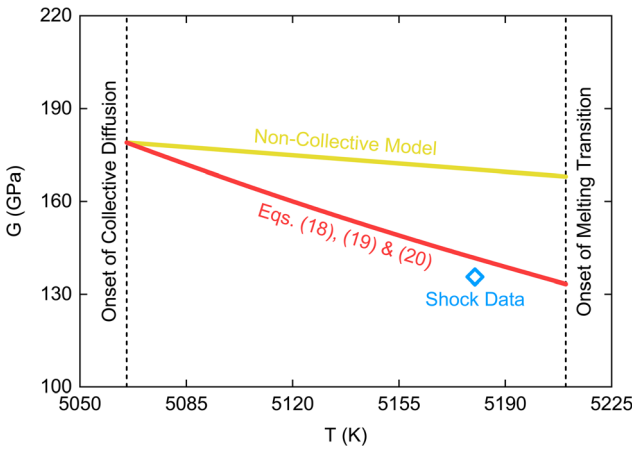

Fig. 8 DSL-SMM-ECNLE analyses for the shear modulus of hcp-iron at 230 GPa. Data from the non-collective model of Ikuta *et al.*[83] and the shock-wave experiment of Zhang *et al.*[25] are also included for comparison.

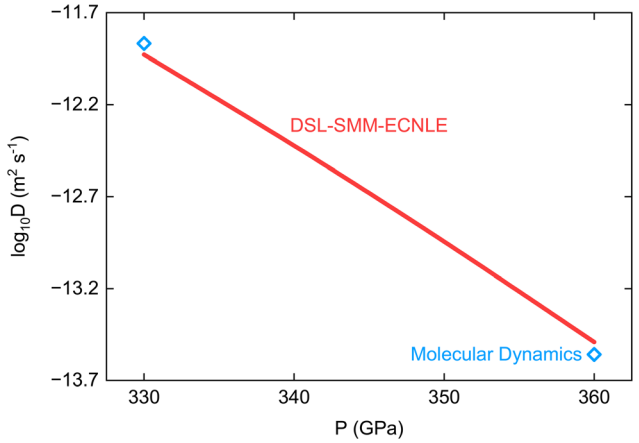

Fig. 9 The diffusivity of hcp-iron along the 6000 K isotherm derived from DSL-SMM-ECNLE approximations and molecular dynamics computations.[25,113]

$$F_{\rm B} = F_{\rm dyn}(r_{\rm B}) - F_{\rm dyn}(r_{\rm L}), \quad (25)$$

where $r_{\rm B}$ and $r_{\rm L}$ represent the maximum and minimum free-energy points. Eqn (25) helps us calculate the structural relaxation time τ_α by the modified Kramers theory,[110]

$$\tau_\alpha = \tau_{\rm s}\left[1+\frac{2\pi}{\sqrt{|K_{\rm B}K_{\rm L}|}}\frac{\theta}{\sigma^2}\exp\left(\frac{F_{\rm B}}{\theta}\right)\right], \quad (26)$$

where $K_{\rm B} = (\partial^2 F_{\rm dyn}/\partial r^2)_{r=r_{\rm B}}$, $K_{\rm L} = (\partial^2 F_{\rm dyn}/\partial r^2)_{r=r_{\rm L}}$, and $\tau_{\rm s}$ is the short relaxation timescale. Since the non-Arrhenius behaviors of metallic systems are much weaker than those of molecular, polymeric, and pharmaceutical liquids,[111] we do not include the elastic barrier in eqn (26). Besides, the strong coupling between relaxation and diffusion in transition metals enables us to deduce the diffusivity D from the Einstein random-walk law,[37,112]

$$D = \frac{\left(r_{\rm B}-r_{\rm L}\right)^2}{6\tau_\alpha}. \quad (27)$$

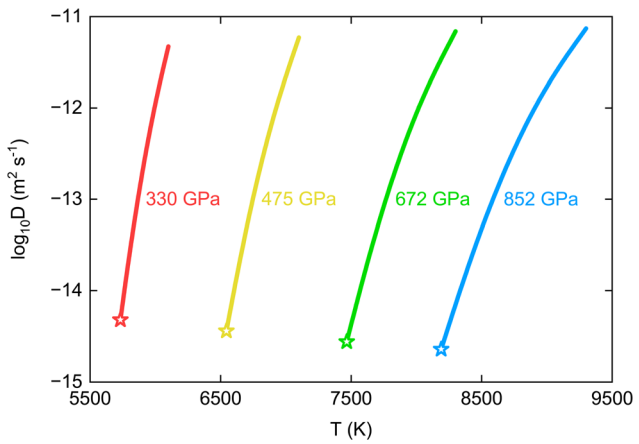

Fig. 10 DSL-SMM-ECNLE outputs for the diffusivity of hcp-iron under extreme conditions relevant to Earth and super-Earth inner cores. The beginning of collective motion is marked by the open star.

Eqn (27) tells us how D depends on ϕ and σ. To transform ϕ into P and T, we employ eqn (18) and (20). The σ variation is inferred from the continuous condition of the shear modulus as

$$\sigma = \sqrt[3]{\frac{6k_B\phi_c T_c}{\pi G_c}\left[1+\frac{36}{5}\frac{\phi_c{}^2(1+\phi_c)}{(1-\phi_c)^3}\right]}, \quad (28)$$

where k_B is the Boltzmann constant.

Fig. 9 shows compression effects on the self-diffusion coefficient of hcp-iron at 6000 K. According to our numerical calculations, D drops considerably from $10^{-11.93}$ m^2 s^{-1} at 330 GPa to $10^{-13.49}$ m^2 s^{-1} at 360 GPa. This change aligns quantitatively well with atomistic simulations. Fitting the MSDs data of Zhang *et al.*[25] with a linear function between 200 and 250 ps gives us $D = 10^{-11.87}$ m^2 s^{-1} near Earth's core-mantle boundary. Additionally, we find $D = 10^{-13.56}$ m^2 s^{-1} from the latest study of Xu *et al.*[113] on the viscosity of iron and iron-based alloys at Earth's center. These numbers affirm the accuracy of the DSL-SMM-ECNLE approach.

Fig. 10 depicts how hcp-iron atoms diffuse in rocky planets. Along the dynamic boundary between collective and non-collective phases, we observe a slight decrease in the diffusion coefficient from $10^{-14.32}$ m^2 s^{-1} at 330 GPa to $10^{-14.64}$ m^2 s^{-1} at 852 GPa. This tendency can be explained by the shortening of the effective diameter during compression. As shown in eqn (28), σ is a decreasing function of P due to the pressure-induced shear hardening of the hcp lattice. The negative σ–P correlation can also be obtained from the simulated radial distribution function, where compressive forces push the contact peak towards lower r-values.[114] Since D is proportional to σ^2 [eqn (27)], our system becomes less diffusive along the T_c–P curve. It should be noted that the D reduction we discuss here does not stem from the structural relaxation of iron atoms because collectivization is an isochronal process in the DSL-SMM-ECNLE picture. Eqn (26) indicates that the onset of collective diffusion is marked by $\tau_\alpha = 10^{-6.41}$ s. Our theoretical results promise to facilitate upcoming research projects on the rheological properties of Earth and super-Earth inner cores since the diffusivity, viscosity, and anelasticity of planet-forming materials are intimately connected.[113,115]

Author contributions

Tran Dinh Cuong: conceptualization, methodology, investigation, writing – original draft, writing-review & editing, visualization. Anh D. Phan: resources, supervision.

Conflicts of interest

The authors declare that they have no known competing financial interests or personal relationships that could have appeared to influence the work reported in this paper.

Data availability

This is a pure theoretical study. All physical quantities are expressed in explicit analytical forms.

Acknowledgements

We use the free version of Grammarly to avoid spelling and grammatical errors.

References

1 Y. He, S. Sun, D. Y. Kim, B. G. Jang, H. Li and H. K. Mao, Superionic iron alloys and their seismic velocities in Earth's inner core, *Nature*, 2022, **602**, 258–262.
2 J. A. Hernandez, M. Bethkenhagen, S. Ninet, M. French, A. Benuzzi-Mounaix, F. Datchi, M. Guarguaglini, F. Lefevre, F. Occelli, R. Redmer, T. Vinci and A. Ravasio, Melting curve of superionic ammonia at planetary interior conditions, *Nat. Phys.*, 2023, **19**, 1280–1285.
3 A. Forestier, G. Weck, F. Datchi, S. Ninet, G. Garbarino, M. Mezouar and P. Loubeyre, X-ray signature of the superionic transition in warm dense fcc water ice, *Phys. Rev. Lett.*, 2025, **134**, 076102.
4 K. de Villa, F. Gonzalez-Cataldo and B. Militzer, Double superionicity in icy compounds at planetary interior conditions, *Nat. Commun.*, 2023, **14**, 7580.
5 S. Pan, T. Huang, A. Vazan, Z. Liang, C. Liu, J. Wang, C. J. Pickard, H. T. Wang, D. Xing and J. Sun, Magnesium oxide-water compounds at megabar pressure and implications on planetary interiors, *Nat. Commun.*, 2023, **14**, 1165.
6 S. Sun, Y. He, J. Yang, Y. Lin, J. Li, D. Y. Kim, H. Li and H. K. Mao, Superionic effect and anisotropic texture in Earth's inner core driven by geomagnetic field, *Nat. Commun.*, 2023, **14**, 1656.
7 A. B. Belonoshko, T. Lukinov, J. Fu, J. Zhao, S. Davis and S. I. Simak, Stabilization of body-centred cubic iron under inner-core conditions, *Nat. Geosci.*, 2017, **10**, 312–316.
8 A. B. Belonoshko, J. Fu, T. Bryk, S. I. Simak and M. Mattesini, Low viscosity of the Earth's inner core, *Nat. Commun.*, 2019, **10**, 2483.
9 A. B. Belonoshko, S. I. Simak, W. Olovsson and O. Y. Vekilova, Elastic properties of body-centered cubic iron in Earth's inner core, *Phys. Rev. B*, 2022, **105**, L180102.
10 T. D. Cuong and A. D. Phan, Effects of cooperative diffusion on rheological and mechanical behavior of bcc Fe: A combined approach using elastically collective nonlinear Langevin equation theory and statistical moment method, *Phys. Rev. B*, 2024, **109**, 054112.
11 G. S. Smirnov, O. E. Peil, A. V. Ruban, S. I. Simak and A. B. Belonoshko, Impact of magnetism on Fe phase diagram under extreme conditions, *Phys. Rev. Mater.*, 2025, **9**, L040601.
12 R. Hrubiak, Y. Meng and G. Shen, Experimental evidence of a body centered cubic iron at the Earth's core condition, *arXiv*, 2018, preprint, arXiv:1804.05109, DOI: 10.48550/arXiv.1804.05109.
13 Z. Konopkova, E. Edmund, O. B. Ball, A. Dewaele, H. Ginestet, R. J. Husband, N. Jaisle, C. Strohm, M. S. Anae, D. Antonangeli, K. Appel, M. Baron, S. Boccato, K. Buakor, J. Chantel, H. Cynn, A. P. Dwivedi,

L. Ehm, K. Glazyrin, H. Graafsma, E. Koemets, T. Laurus, H. Marquardt, B. Massani, J. D. McHardy, M. I. McMahon, V. Prakapenka, J. Sztuk-Dambietz, M. Tang, T. Xie, Z. Younes, U. Zastrau, A. F. Goncharov, C. Prescher, R. S. McWilliams, G. Morard and S. Merkel, Observation of body-centered cubic iron above 200 gigapascals, *arXiv*, 2025, preprint, arXiv:2505.15397, DOI: 10.48550/arXiv.2505.15397.

14 Y. Ping, F. Coppari, D. G. Hicks, B. Yaakobi, D. E. Fratanduono, S. Hamel, J. H. Eggert, J. R. Rygg, R. F. Smith, D. C. Swift, D. G. Braun, T. R. Boehly and G. W. Collins, Solid iron compressed up to 560 GPa, *Phys. Rev. Lett.*, 2013, **111**, 065501.

15 S. J. Turneaure, S. M. Sharma and Y. M. Gupta, Crystal structure and melting of Fe shock compressed to 273 GPa: In situ X-ray diffraction, *Phys. Rev. Lett.*, 2020, **125**, 215702.

16 R. G. Kraus, R. J. Hemley, S. J. Ali, J. L. Belof, L. X. Benedict, J. Bernier, D. Braun, R. E. Cohen, G. W. Collins, F. Coppari, M. P. Desjarlais, D. Fratanduono, S. Hamel, A. Krygier, A. Lazicki, J. Mcnaney, M. Millot, P. C. Myint, M. G. Newman, J. R. Rygg, D. M. Sterbentz, S. T. Stewart, L. Stixrude, D. C. Swift, C. Wehrenberg and J. H. Eggert, Measuring the melting curve of iron at super-Earth core conditions, *Science*, 2022, **375**, 202–205.

17 C. J. Wu, L. X. Benedict, P. C. Myint, S. Hamel, C. J. Prisbrey and J. R. Leek, Wide-ranged multiphase equation of state for iron and model variations addressing uncertainties in high-pressure melting, *Phys. Rev. B*, 2023, **108**, 014102.

18 S. Balugani, J. A. Hernandez, N. Sevelin-Radiguet, O. Mathon, V. Recoules, J. J. Kas, D. E. Eakins, H. Doyle, A. Ravasio and R. Torchio, New constraints on the melting temperature and phase stability of shocked iron up to 270 GPa probed by ultrafast X-ray absorption spectroscopy, *Phys. Rev. Lett.*, 2024, **133**, 254101.

19 A. J. Schultz, S. G. Moustafa and D. A. Kofke, No system-size anomalies in entropy of bcc iron at Earth's inner-core conditions, *Sci. Rep.*, 2018, **8**, 7295.

20 F. Gonzalez-Cataldo and B. Militzer, Ab initio determination of iron melting at terapascal pressures and super-Earths core crystallization, *Phys. Rev. Res.*, 2023, **5**, 033194.

21 I. A. Kruglov, A. V. Yanilkin, Y. Propad, A. B. Mazitov, P. Rachitskii and A. R. Oganov, Crystal structure prediction at finite temperatures, *npj Comput. Mater.*, 2023, **9**, 197.

22 F. Wu, S. Wu, C. Z. Wang, K. M. Ho, R. M. Wentzcovitch and Y. Sun, Melting temperature of iron under the Earth's inner core condition from deep machine learning, *Geosci. Front.*, 2024, **15**, 101925.

23 L. Zhao, V. Lordi and A. Samanta, Melting point of iron at high pressure: An assessment of uncertainties and effect of electronic temperature, *Appl. Phys. Lett.*, 2024, **124**, 144105.

24 A. B. Belonoshko, J. Fu and G. Smirnov, Free energies of iron phases at high pressure and temperature: Molecular dynamics study, *Phys. Rev. B*, 2021, **104**, 104103.

25 Y. Zhang, Y. Wang, Y. Huang, J. Wang, Z. Liang, L. Hao, Z. Gao, J. Li, Q. Wu, H. Zhang, Y. Liu, J. Sun and J. F. Lin, Collective motion in hcp-Fe at Earth's inner core conditions, *Proc. Natl. Acad. Sci. U. S. A.*, 2023, **120**, e2309952120.

26 S. Mazevet, R. Musella and F. Guyot, The fate of planetary cores in giant and ice-giant planets, *Astron. Astrophys.*, 2019, **631**, L4.

27 A. Boujibar, P. Driscoll and Y. Fei, Super-Earth internal structures and initial thermal states, *J. Geophys. Res.: Planets*, 2020, **125**, e2019JE006124.

28 A. Gray-Weale and P. A. Madden, Dynamical arrest in superionic crystals and supercooled liquids, *J. Phys. Chem. B*, 2004, **108**, 6624–6633.

29 A. Gray-Weale and P. A. Madden, The energy landscape of a fluorite-structured superionic conductor, *J. Phys. Chem. B*, 2004, **108**, 6634–6642.

30 H. Zhang, X. Wang, A. Chremos and J. F. Douglas, Superionic UO_2: A model anharmonic crystalline material, *J. Chem. Phys.*, 2019, **150**, 174506.

31 H. Zhang, X. Wang and J. F. Douglas, Localization model description of diffusion and structural relaxation in superionic crystalline UO_2, *J. Chem. Phys.*, 2019, **151**, 071101.

32 K. Koperwas, A. Grzybowski, K. Grzybowska, Z. Wojnarowska, J. Pionteck, A. P. Sokolov and M. Paluch, Pressure coefficient of the glass transition temperature in the thermodynamic scaling regime, *Phys. Rev. E: Stat., Nonlinear, Soft Matter Phys.*, 2012, **86**, 041502.

33 T. D. Cuong and A. D. Phan, Reconstructing the phase diagram of iron in the terapascal region via the statistical moment method, *Phys. Rev. B*, 2023, **108**, 134111.

34 R. Boehler, Temperatures in the Earth's core from melting-point measurements of iron at high static pressures, *Nature*, 1993, **363**, 534–536.

35 S. Anzellini, A. Dewaele, M. Mezouar, P. Loubeyre and G. Morard, Melting of iron at Earth's inner core boundary based on fast X-ray diffraction, *Science*, 2013, **340**, 464–466.

36 R. Sinmyo, K. Hirose and Y. Ohishi, Melting curve of iron to 290 GPa determined in a resistance-heated diamond-anvil cell, *Earth Planet. Sci. Lett.*, 2019, **510**, 45–52.

37 H. Zhang, M. Khalkhali, Q. Liu and J. F. Douglas, String-like cooperative motion in homogeneous melting, *J. Chem. Phys.*, 2013, **138**, 12A538.

38 V. A. Annamareddy, P. K. Nandi, X. Mei and J. Eapen, Waxing and waning of dynamical heterogeneity in the superionic state, *Phys. Rev. E: Stat., Nonlinear, Soft Matter Phys.*, 2014, **89**, 010301(R).

39 A. Annamareddy and J. Eapen, Mobility propagation and dynamic facilitation in superionic conductors, *J. Chem. Phys.*, 2015, **143**, 194502.

40 P. C. M. Fossati, P. A. Burr, M. W. D. Cooper, C. O. T. Galvin and R. W. Grimes, Superionic transition in uranium dioxide: Insights from molecular dynamics and lattice dynamics simulations, *Phys. Rev. Mater.*, 2024, **8**, 115404.

41 B. A. P. Betancourt, P. Z. Hanakata, F. W. Starr and J. F. Douglas, Quantitative relations between cooperative

motion, emergent elasticity, and free volume in model glass-forming polymer materials, *Proc. Natl. Acad. Sci. U. S. A.*, 2015, **112**, 2966–2971.
42 G. Adam and J. H. Gibbs, On the temperature dependence of cooperative relaxation properties in glass-forming liquids, *J. Chem. Phys.*, 1965, **43**, 139–146.
43 T. D. Cuong and A. D. Phan, Superionic UO_2 crystal: How to model its relaxation and diffusion via a microscopic theory of glass-forming liquids, *Phys. Rev. E*, 2025, **111**, 015434.
44 P. Lunkenheimer, A. Loidl, B. Riechers, A. Zaccone and K. Samwer, Thermal expansion and the glass transition, *Nat. Phys.*, 2023, **19**, 694–699.
45 J. W. P. Schmelzer, Kinetic criteria of glass formation and the pressure dependence of the glass transition temperature, *J. Chem. Phys.*, 2012, **136**, 074512.
46 K. Koperwas, A. Grzybowski, K. Grzybowska, Z. Wojnarowska and M. Paluch, Effects of dynamic heterogeneity and density scaling of molecular dynamics on the relationship among thermodynamic coefficients at the glass transition, *J. Chem. Phys.*, 2015, **143**, 024502.
47 M. A. Korneva and S. V. Starikov, Atomistic simulation of a superionic transition in fluorite type structures UO_2, UN_2, TiH_2, *J. Phys.: Conf. Ser.*, 2016, **774**, 012037.
48 N. Gnan, T. B. Schrøder, U. R. Pedersen, N. P. Bailey and J. C. Dyre, Pressure-energy correlations in liquids. IV. "Isomorphs" in liquid phase diagrams, *J. Chem. Phys.*, 2009, **131**, 234504.
49 D. Gundermann, U. R. Pedersen, T. Hecksher, N. P. Bailey, B. Jakobsen, T. Christensen, N. B. Olsen, T. B. Schrøder, D. Fragiadakis, R. Casalini, C. M. Roland, J. C. Dyre and K. Niss, Predicting the density-scaling exponent of a glass-forming liquid from Prigogine–Defay ratio measurements, *Nat. Phys.*, 2011, **7**, 816–821.
50 J. C. Dyre, Hidden scale invariance in condensed matter, *J. Phys. Chem. B*, 2014, **118**, 10007–10024.
51 L. Bøhling, N. P. Bailey, T. B. Schrøder and J. C. Dyre, Estimating the density-scaling exponent of a monatomic liquid from its pair potential, *J. Chem. Phys.*, 2014, **140**, 124510.
52 F. Kaskosz, K. Koperwas, A. Grzybowski and M. Paluch, The origin of the density scaling exponent for polyatomic molecules and the estimation of its value from the liquid structure, *J. Chem. Phys.*, 2023, **158**, 144503.
53 M. Paluch, B. Yao, J. Pionteck and Z. Wojnarowska, Predicting the density-scaling exponent of a glass-forming liquid from complex dielectric permittivity measurements, *Phys. Rev. Lett.*, 2023, **131**, 086101.
54 K. Koperwas, A. Grzybowski and M. Paluch, Exploring the connection between the density-scaling exponent and the intermolecular potential for liquids on the basis of computer simulations of quasireal model systems, *Phys. Rev. E*, 2020, **101**, 012613.
55 T. C. Ransom, M. Ahart, R. J. Hemley and C. M. Roland, Vitrification and density scaling of polyurea at pressures up to 6 GPa, *Macromolecules*, 2017, **50**, 8274–8278.
56 T. C. Ransom and W. F. Oliver, Glass transition temperature and density scaling in cumene at very high pressure, *Phys. Rev. Lett.*, 2017, **119**, 025702.
57 H. K. Hieu, Systematic prediction of high-pressure melting curves of transition metals, *J. Appl. Phys.*, 2014, **116**, 163505.
58 T. D. Cuong, N. Q. Hoc, N. D. Trung, N. T. Thao and A. D. Phan, Theoretical predictions of melting behaviors of hcp iron up to 4000 GPa, *Phys. Rev. B*, 2022, **106**, 094103.
59 N. Q. Hoc, N. D. Trung, N. N. Thang, N. V. Hoang and L. T. Lam, Melting curves of $MgSiO_3$ and $CaSiO_3$ perovskites with cubic structure at extreme conditions, *J. Appl. Phys.*, 2024, **136**, 045103.
60 N. Tang and V. V. Hung, Investigation of the thermodynamic properties of anharmonic crystals by the momentum method. I. General results for face-centred cubic crystals, *Phys. Status Solidi B*, 1988, **149**, 511–519.
61 K. Masuda-Jindo, V. V. Hung and P. D. Tam, Thermodynamic quantities of metals investigated by an analytic statistical moment method, *Phys. Rev. B: Condens. Matter Mater. Phys.*, 2003, **67**, 094301.
62 K. Masuda-Jindo, S. R. Nishitani and V. V. Hung, hcp-bcc structural phase transformation of titanium: Analytic model calculations, *Phys. Rev. B: Condens. Matter Mater. Phys.*, 2004, **70**, 184122.
63 Y. P. Varshni and F. J. Bloore, Rydberg function as an interatomic potential for metals, *Phys. Rev.*, 1963, **129**, 115.
64 P. Vinet, J. H. Rose, J. Ferrante and J. R. Smith, Universal features of the equation of state of solids, *J. Phys.: Condens. Matter*, 1989, **1**, 1941.
65 F. Coppari, D. E. Fratanduono, M. Millot, R. G. Kraus, A. Lazicki, J. R. Rygg, R. F. Smith and J. H. Eggert, X-ray diffraction measurements and pressure determination in nanosecond compression of solids up to 600 GPa, *Phys. Rev. B*, 2022, **106**, 134105.
66 L. Stixrude and R. E. Cohen, First principles investigation of bcc, fcc, and hcp phases of iron, *AIP Conf. Proc.*, 1994, **309**, 911–914.
67 K. Hakim, A. Rivoldini, T. V. Hoolst, S. Cottenier, J. Jaeken, T. Chust and G. Steinle-Neumann, A new ab initio equation of state of hcp-Fe and its implication on the interior structure and mass-radius relations of rocky super-Earths, *Icarus*, 2018, **313**, 61–78.
68 G. Leibfried and W. Ludwig, Theory of anharmonic effects in crystals, *Solid State Phys.*, 1961, **12**, 275–444.
69 A. Einstein, Die plancksche theorie der strahlung und die theorie der spezifischen wärme, *Ann. Phys.*, 1907, **327**, 180–190.
70 L. V. Al'tshuler, S. B. Kormer, M. I. Brazhnik, L. A. Vladimirov, M. P. Speranskaya and A. I. Funtikov, The isentropic compressibility of aluminum, copper, lead, and iron at high pressures, *Sov. Phys. -JETP*, 1960, **11**, 766.
71 T. S. Duffy and T. J. Ahrens, Thermal expansion of mantle and core materials at very high pressures, *Geophys. Res. Lett.*, 1993, **20**, 1103–1106.
72 F. Simon and G. Glatzel, Bemerkungen zur schmelzdruckkurve, *Z. Anorg. Allg. Chem.*, 1929, **178**, 309–316.
73 G. Morard, S. Boccato, A. D. Rosa, S. Anzellini, F. Miozzi, L. Henry, G. Garbarino, M. Mezouar, M. Harmand, F. Guyot, E. Boulard, I. Kantor, T. Irifune and R. Torchio,

Solving controversies on the iron phase diagram under high pressure, *Geophys. Res. Lett.*, 2018, **45**, 11074–11082.
74 G. Aquilanti, A. Trapananti, A. Karandikar, I. Kantor, C. Marini, O. Mathon, S. Pascarelli and R. Boehler, Melting of iron determined by X-ray absorption spectroscopy to 100 GPa, *Proc. Natl. Acad. Sci. U. S. A.*, 2015, **112**, 12042–12045.
75 J. M. Jackson, W. Sturhahn, M. Lerche, J. Zhao, T. S. Toellner, E. E. Alp, S. V. Sinogeikin, J. D. Bass, C. A. Murphy and J. K. Wicks, Melting of compressed iron by monitoring atomic dynamics, *Earth Planet. Sci. Lett.*, 2013, **362**, 143–150.
76 D. Zhang, J. M. Jackson, J. Zhao, W. Sturhahn, E. E. Alp, M. Y. Hu, T. S. Toellner, C. A. Murphy and V. B. Prakapenka, Temperature of Earth's core constrained from melting of Fe and $Fe_{0.9}Ni_{0.1}$ at high pressures, *Earth Planet. Sci. Lett.*, 2016, **447**, 72–83.
77 R. Qiu, Q. Zeng, H. Wang, D. Kang, X. Yu and J. Dai, Anomalous thermal transport across the superionic transition in ice, *Chin. Phys. Lett.*, 2023, **40**, 116301.
78 J. Li, Q. Wu, J. Li, T. Xue, Y. Tan, X. Zhou, Y. Zhang, Z. Xiong, Z. Gao and T. Sekine, Shock melting curve of iron: A consensus on the temperature at the Earth's inner core boundary, *Geophys. Res. Lett.*, 2020, **47**, e2020GL087758.
79 M. Hou, J. Liu, Y. Zhang, X. Du, H. Dong, L. Yan, J. Wang, L. Wang and B. Chen, Melting of iron explored by electrical resistance jump up to 135 GPa, *Geophys. Res. Lett.*, 2021, **48**, e2021GL095739.
80 A. M. Dziewonski and D. L. Anderson, Preliminary reference Earth model, *Phys. Earth Planet. Inter.*, 1981, **25**, 297–356.
81 B. L. N. Kennett, E. R. Engdahl and R. Buland, Constraints on seismic velocities in the Earth from traveltimes, *Geophys. J. Int.*, 1995, **122**, 108–124.
82 H. Tkalcic and T. S. Pham, Shear properties of Earth's inner core constrained by a detection of *J* waves in global correlation wavefield, *Science*, 2018, **362**, 329–332.
83 D. Ikuta, E. Ohtani, H. Fukui, T. Sakai, D. Ishikawa and A. Q. R. Baron, Sound velocity of hexagonal close-packed iron to the Earth's inner core pressure, *Nat. Commun.*, 2022, **13**, 7211.
84 S. C. Singh, M. A. J. Taylor and J. P. Montagner, On the presence of liquid in Earth's inner core, *Science*, 2000, **287**, 2471–2474.
85 B. Martorell, L. Vocadlo, J. Brodholt and I. G. Wood, Strong premelting effect in the elastic properties of hcp-Fe under inner-core conditions, *Science*, 2013, **342**, 466–468.
86 W. Wang, Y. Li, J. P. Brodholt, L. Vocadlo, M. J. Walter and Z. Wu, Strong shear softening induced by superionic hydrogen in Earth's inner core, *Earth Planet. Sci. Lett.*, 2021, **568**, 117014.
87 Z. Li and S. Scandolo, Elasticity and viscosity of hcp iron at Earth's inner core conditions from machine learning-based large-scale atomistic simulations, *Geophys. Res. Lett.*, 2022, **49**, e2022GL101161.
88 J. K. Percus and G. J. Yevick, Analysis of classical statistical mechanics by means of collective coordinates, *Phys. Rev.*, 1958, **110**, 1.
89 B. N. Miller, Elastic moduli of a fluid of rigid spheres, *J. Chem. Phys.*, 1969, **50**, 2733–2740.
90 S. Khrapak, N. P. Kryuchkov, L. A. Mistryukova and S. O. Yurchenko, From soft-to hard-sphere fluids: Crossover evidenced by high-frequency elastic moduli, *Phys. Rev. E*, 2021, **103**, 052117.
91 A. S. Makarov, Y. P. Mitrofanov, G. V. Afonin, N. P. Kobelev and V. A. Khonik, Predicting temperature dependence of the shear modulus of metallic glasses using calorimetric data, *Scr. Mater.*, 2019, **168**, 10–13.
92 T. D. Cuong and A. D. Phan, Effects of hydrostatic compression and kinetic vitrification on structural relaxation behaviors of amorphous drugs: How to predict them via simple theoretical models?, *RSC Adv.*, 2025, **15**, 25675–25693.
93 G. Righi, T. E. Lockard, R. E. Rudd, M. A. Meyers and H. S. Park, Design of high-pressure iron Rayleigh–Taylor strength experiments for the National Ignition Facility, *J. Appl. Phys.*, 2022, **131**, 145902.
94 O. R. Deluigi and E. M. Bringa, Mechanical properties of hcp Fe at high pressures and temperatures from large-scale molecular dynamics simulations, *J. Appl. Phys.*, 2024, **136**, 195901.
95 K. Hirose, B. Wood and L. Vocadlo, Light elements in the Earth's core, *Nat. Rev. Earth Environ.*, 2021, **2**, 645–658.
96 R. L. Akeson, X. Chen, D. Ciardi, M. Crane, J. Good, M. Harbut, E. Jackson, S. R. Kane, A. C. Laity, S. Leifer, M. Lynn, D. L. McElroy, M. Papin, P. Plavchan, S. V. Ramirez, R. Rey, K. von Braun, M. Wittman, M. Abajian, B. Ali, C. Beichman, A. Beekley, G. B. Berriman, S. Berukoff, G. Bryden, B. Chan, S. Groom, C. Lau, A. N. Payne, M. Regelson, M. Saucedo, M. Schmitz, J. Stauffer, P. Wyatt and A. Zhang, The NASA exoplanet archive: Data and tools for exoplanet research, *Publ. Astron. Soc. Pac.*, 2013, **125**, 989–999.
97 C. H. Lineweaver and A. Chopra, The habitability of our Earth and other Earths: Astrophysical, geochemical, geophysical, and biological limits on planet habitability, *Annu. Rev. Earth Planet. Sci.*, 2012, **40**, 597–623.
98 Y. Zhang and J. F. Lin, Molten iron in Earth-like exoplanet cores, *Science*, 2022, **375**, 146–147.
99 L. Stixrude, Melting in super-Earths, *Philos. Trans. R. Soc., A*, 2014, **372**, 20130076.
100 S. Stanley and J. Bloxham, Numerical dynamo models of Uranus' and Neptune's magnetic fields, *Icarus*, 2006, **184**, 556–572.
101 K. M. Soderlund and S. Stanley, The underexplored frontier of ice giant dynamos, *Philos. Trans. R. Soc., A*, 2020, **378**, 20190479.
102 M. Rams-Baron, R. Jachowicz, E. Boldyreva, D. Zhou, W. Jamroz and M. Paluch, *Amorphous Drugs: Benefits and Challenges*, Springer, Cham, 2018.

103 S. M. Wahl, H. F. Wilson and B. Militzer, Solubility of iron in metallic hydrogen and stability of dense cores in giant planets, *Astrophys. J.*, 2013, **773**, 95.
104 National Academies of Sciences, Engineering, and Medicine, *Origins, Worlds, and Life: A Decadal Strategy for Planetary Science and Astrobiology 2023–2032*, National Academies Press, Washington (DC), 2023.
105 M. Ghosh, S. Zhang, L. Hu and S. X. Hu, Cooperative diffusion in body-centered cubic iron in Earth and super-Earths' inner core conditions, *J. Phys.: Condens. Matter*, 2023, **35**, 154002.
106 Z. Li and S. Scandolo, Competing phases of iron at Earth's core conditions from deep-learning-aided ab-initio simulations, *Geophys. Res. Lett.*, 2024, **51**, e2024GL110357.
107 T. D. Cuong and A. D. Phan, Modeling the elastic properties of bcc iron in Earth's core by quantum statistical physics, *Vacuum*, 2025, **237**, 114116.
108 Z. Wojnarowska, M. Musiał, M. Dzida and M. Paluch, Experimental evidence for a state-point-independent density-scaling exponent in ionic liquids, *Phys. Rev. Lett.*, 2019, **123**, 125702.
109 K. S. Schweizer, Derivation of a microscopic theory of barriers and activated hopping transport in glassy liquids and suspensions, *J. Chem. Phys.*, 2005, **123**, 244501.
110 P. Hanggi, P. Talkner and M. Borkovec, Reaction-rate theory: Fifty years after Kramers, *Rev. Mod. Phys.*, 1990, **62**, 251.
111 A. D. Phan, A. Zaccone, V. D. Lam and K. Wakabayashi, Theory of pressure-induced rejuvenation and strain hardening in metallic glasses, *Phys. Rev. Lett.*, 2021, **126**, 025502.
112 J. Zhang, J. F. Douglas and H. Zhang, String-like collective motion mediates the martensitic α–β transition in titanium, *J. Chem. Phys.*, 2025, **163**, 044504.
113 Y. Xu, Y. He, S. Sun, W. Zhang, W. Dai, D. Y. Kim and H. Li, Viscosities of hcp iron alloys under Earth's inner core conditions, *Geosci. Front.*, 2025, **16**, 101935.
114 L. E. Gonzalez and D. J. Gonzalez, Structure and dynamics in liquid iron at high pressure and temperature. A first principles study, *J. Geophys. Res.: Solid Earth*, 2023, **128**, e2022JB025119.
115 H. Tkalcic, A. B. Belonoshko, J. B. Muir, M. Mattesini, L. Moresi and L. Waszek, Imaging the top of the Earth's inner core: A present-day flow model, *Sci. Rep.*, 2024, **14**, 8999.